Journal Pre-proofs

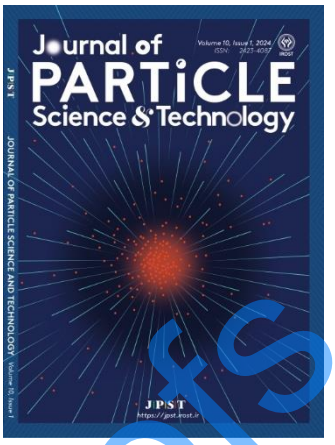

Extending the allowable exposure time of rotating X-ray anodes via an embedded lithium pulsating heat pipe: A 3D multiphase analysis

Mohsen Amini, Faramarz Sarhaddi, Hassan Azarkish

DOI: https://doi.org/10.22104/jpst.2026.8247.1291
Manuscript number: JPST-2605-1291

To appear in: *Journal of Particle Science and Technology (JPST)*

Received Date: 13 May 2026
Received Date in revised form: 8 June 2026
Accepted Date: 17 June 2026

Please cite this article as: Amini, M., Sarhaddi, F., Azarkish, H., Extending the allowable exposure time of rotating X-ray anodes via an embedded lithium pulsating heat pipe: A 3D multiphase analysis, *Journal of Particle Science and Technology* (2025), doi: https://doi.org/10.22104/jpst.2026.8247.1291

Extending the Allowable Exposure Time of Rotating X-ray Anodes via an Embedded Lithium Pulsating Heat Pipe: A 3D Multiphase Analysis

Mohsen Amini, Faramarz Sarhaddi*, Hassan Azarkish

Department of Mechanical Engineering, University of Sistan and Baluchestan, Zahedan, Iran

Abstract

Thermal management of high-power X-ray rotating anodes is strictly constrained by the intense, localized heat fluxes generated during brief exposure times. This study proposes the integration of a lithium-based Rotating Pulsating Heat Pipe (RPHP) into the anode and investigates its transient thermal-hydraulic performance using a Volume of Fluid (VOF) multiphase model, which is heavily influenced by both extreme centrifugal forces and the intense heat flux applied during the exposure time. The results reveal a fundamental thermodynamic trade-off governing the optimal rotational speed: while higher rotational speeds enhance internal fluid circulation as well as latent and sensible heat transport, they simultaneously generate massive hydrostatic pressures that cause a significant transient delay in the phase-change (boiling) process. Consequently, the maximum allowable exposure time exhibits a non-monotonic dependence on the rotational speed. A case study based on the RAD-14 X-ray tube was investigated with a heat input of 20 kW on a minimum focal spot size (0.3 mm). A critical temperature limit of 2200 K was defined to evaluate and compare the allowable exposure times across different configurations. Compared to a conventional solid anode (which is limited to an exposure time of 0.436 s), the RPHP integration at 8500 RPM achieves optimal thermal performance, extending the allowable exposure time to 0.706 s (a 62% increment). However, further increasing the speed to 10000 RPM exacerbates the pressure-induced boiling retardation, leading to an exposure time of 0.619 s (a 42% increment relative to the solid base, but a 12% reduction compared to the 8500 RPM peak).

Keywords: Rotating anode X-ray tube, Rotating pulsating heat pipe (RPHP), VOF, Thermal management

1. Introduction

Effective thermal management remains one of the primary engineering bottlenecks in modern high performance computed tomography (CT) systems. In rotating anode X-ray tubes (as schematically shown in Fig. 1), over 99% of the electron beam energy becomes intensely localized heat at the focal track, creating sharp transient temperature rises that strictly limit the exposure time, the maximum deliverable peak power, and the minimum focal spot size (three parameters central to radiographic performance).

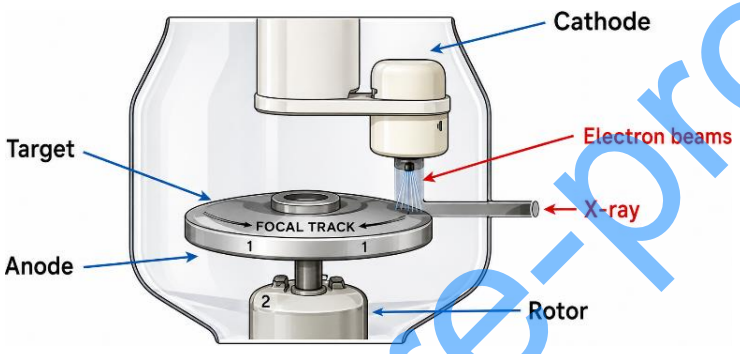

Fig 1. Schematic of a rotating anode X-ray tube [1].

In clinical practice, the thermal operational limits of rotating X-ray tubes are governed by three standard charts [2]: (1) the radiographic rating chart (which defines the maximum safe exposure settings—input power, and time—for a single exposure to prevent focal track damage), (2) the anode cooling chart (which shows the rate at which the anode assembly dissipates its stored heat, determining the necessary wait time between exposures), and (3) the housing cooling chart (which illustrates the long-term heat dissipation from the entire tube housing, governing the overall duty cycle for continuous operation). Because the anode operates in a high vacuum environment, thermal radiation is the main mode of heat rejection to the surroundings. Consequently, modifications aiming to improve the continuous cooling phase (Chart 2) typically focus on enhancing the radiative heat transfer. For instance, Moon Lee [3] proposed increasing the radiative heat transfer surface area by stepping the back of the anode disk, reporting an increase in the allowable electron beam power from

approximately 75 to 100 kW for a 0.1 s pulse. In another study, Lee [1] conducted a transient thermal analysis to investigate the effect of emissivity on the focal track and rotor assembly. By applying a high-emissivity black coating (0.95) to the back side of the Titanium–Zirconium–Molybdenum alloy (TZM) body, the study demonstrated how the surface treatments can further improve heat dissipation. Other researchers [4] have focused on high-conductivity materials by introducing the use of a synthetic diamond layer beneath the target surface to rapidly conduct heat away from the focal spot.

Additionally, thermal analyses on high-power rotating anodes [5] have revealed that improving thermal conductivity of the anode material, such as using chemical vapor deposition (CVD) tungsten instead of powder metallurgy, can effectively reduce the focal track temperatures. Kumar *et al.* [6] further emphasized through transient thermal analysis during exhaust and degassing processes that insufficient heat rejection in high-vacuum environments can cause severe damage, including sublimation of the tungsten–rhenium target and filament failure.

Recently, Pajovic *et al.* [7] introduced a nanophotonic thermal management approach, demonstrating that patterning the tungsten anode surface with a photonic crystal significantly enhances its total hemispherical emissivity. Similarly, Wang *et al.* [8] optimized the geometric design of the rotating anode by altering the tilt angle of the target disk's backside. They aimed to maximize the radiation view factor between the high-temperature anode and the surrounding tube shell, and the results show increasing the net radiative heat transfer by approximately 40%.

Recognizing the thermal limits of relying solely on radiative heat transfer, Wang *et al.* [9] investigated an active internal cooling strategy for a 3.5 MHU rotating anode equipped with liquid metal bearings. They demonstrated that circulating cooling oil directly into the shaft core significantly reduced thermal strain and prevented bearing seizure.

To overcome these drawbacks and achieve internal heat spreading, Pulsating Heat Pipes (PHPs) present a robust, passive two-phase solution. Originally introduced by Akachi [10], PHP performance strongly depends on channel geometry and operating conditions [11-17]. Recent fundamental studies

have also highlighted the importance of surface morphology; for example, [18] demonstrated that surface roughness and micro-cavities directly govern stable bubble nucleation and the onset of oscillatory motion in PHPs. Furthermore, geometrical optimization has proven highly effective. Yu *et al.* [19] developed a variable-diameter PHP for industrial extruders, deliberately creating internal pressure imbalances to accelerate liquid plug formation and significantly reduce start-up time. Similar structural enhancements, such as cross-bonding and fabric-like internal structures [20], as well as the optimization of operational parameters [21], have been shown to drastically increase the equivalent thermal conductivity of PHPs.

Crucially, PHPs have demonstrated exceptional performance in rotating environments where centrifugal acceleration actively drives condensate return. Preliminary studies by Aboutalebi *et al.* [22] proved that rotational speed significantly delays the dry-out phenomenon. Subsequent investigations into closed-loop PHPs under higher centrifugal accelerations (up to 20g and 800 rpm) revealed that increased rotation enhances phase-change circulation and minimizes thermal resistance, with these improvements peaking when the working fluid and filling ratio are optimally selected [23–25]. Furthermore, practical applications of this concept have been successfully demonstrated, such as Gao *et al.*'s [26] use of PHPs to cool rotating wind turbine components at 17.3 rpm.

Despite the independent progress in X-ray tube thermal management and rotating PHP technology, combining these two domains remains unrealized. As previously noted, approaches based on enhancing radiative heat transfer—such as increasing effective surface area [3], improving emissivity [1, 7], or boosting view factor [8]—primarily influence the anode cooling chart (Chart 2) and cannot, on their own, suppress the severe and highly localized transient temperature spikes generated during short exposures. Recent fundamental investigations [27,28] underscore the destructive nature of these unmitigated transient spikes. Their studies demonstrated that extreme thermal gradients lead to severe thermo-mechanical degradation, including sub-surface cracking and the progressive thermal isolation of individual tungsten grains. This physical degradation severely

restricts internal heat flow, definitively proving that solid-state thermal conduction alone is fundamentally incapable of dissipating localized energy fast enough to prevent focal track erosion and melting. While the use of synthetic diamond layers [4] also offers benefits due to its high thermal conductivity, yet its practical impact is restricted by its small feasible thickness (≈0.5 mm) and the steep rise in cost for thicker layers—while still lacking the fast, deep heat penetration capability characteristic of two-phase PHP mechanisms. On the other hand, active internal cooling concepts [9], face serious practicality issues at high rotational speeds due to mechanical complexity and sealing difficulties in vacuum environments. As a result, a genuine scientific gap persists: no existing method provides a practical, fast response solution for mitigating transient focal track thermal surges within a rotating anode (Chart 1).

While PHPs offer an ideal passive internal cooling mechanism and thrive under centrifugal forces [22-26], their application within the extreme environment of a high-speed X-ray anode (2850–10000 rpm) remains largely unexplored. Most existing numerical investigations of PHPs assume a constant saturation temperature [29-33]. However, in ultra-high-speed rotating environments, intense centrifugal forces elevate the hydrostatic pressure, shifting the nucleation temperature higher and causing a delay in boiling incipience. Additionally, continuous and rapid heat absorption over short durations constantly increases both the pressure and the boiling temperature. Failing to account for this dynamic, pressure-dependent saturation temperature renders traditional numerical models fundamentally inaccurate for capturing the transient two-phase dynamics in X-ray anodes.

To bridge this gap, this study introduces a novel thermal management paradigm: the integration of a rotating pulsating heat pipe (RPHP) directly beneath the focal track of a RAD-14 anode, utilizing the anode disk itself as an integrated condenser. Supported by accurate numerical modeling with pressure-dependent boiling temperature, this study demonstrates how the passive internal heat spreading approach targets the radiographic rating chart directly by accelerating the utilization of the

bulk disk's thermal capacity during the active pulse, offering a highly efficient alternative to the current cooling bottlenecks.

2. Mathematical Modeling and Numerical Method

To ensure effective pulsating flow within the heat pipe, the inner diameter of the channel (d_i) is designed to be within the capillary range [34].

$$0.7\sqrt{\frac{\sigma}{(\rho_l-\rho_v)g}} < d_i < 1.8\sqrt{\frac{\sigma}{(\rho_l-\rho_v)g}} \quad (1)$$

where g is the effective body force, ρ_l and ρ_v are the liquid and vapor densities, and σ is the surface tension. Within the capillary regime, surface tension forces are balanced with body forces, enabling the formation of distinct liquid slugs and vapor plugs. Consequently, the positive pressure generated by rapid vapor bubble expansion drives the fluid from the evaporator toward the condenser. As these bubbles reach the condenser region and shrink or fully collapse due to condensation, the local pressure drops; this allows the dominant body forces to overcome the vapor pressure and propel the liquid back to the evaporator, thereby sustaining the continuous pulsating flow. Based on these considerations, a 0.3 mm×0.3 mm square channel was selected, which is confirmed to be within the capillary range for the operational conditions encountered in this study (2850−10000 rpm).

2.1. Physical Model and Geometry

X-ray tubes are widely utilized for both diagnostic and therapeutic applications; the present study focuses on a diagnostic X-ray tube (RAD-14 type [35]) shown in Fig 2. (a).

In such devices, high-energy electrons bombard a highly concentrated region on the target, known as the focal spot. By rotating the anode around its central axis during the electron bombardment, the thermal energy is swept across a much broader annular area (the focal track) while maintaining a strictly localized X-ray emission source. This dynamic approach mitigates the thermal

bottlenecks inherent in stationary anodes, permitting substantially higher electron currents and consequently, greater X-ray intensities without causing localized degradation or melting of the target.

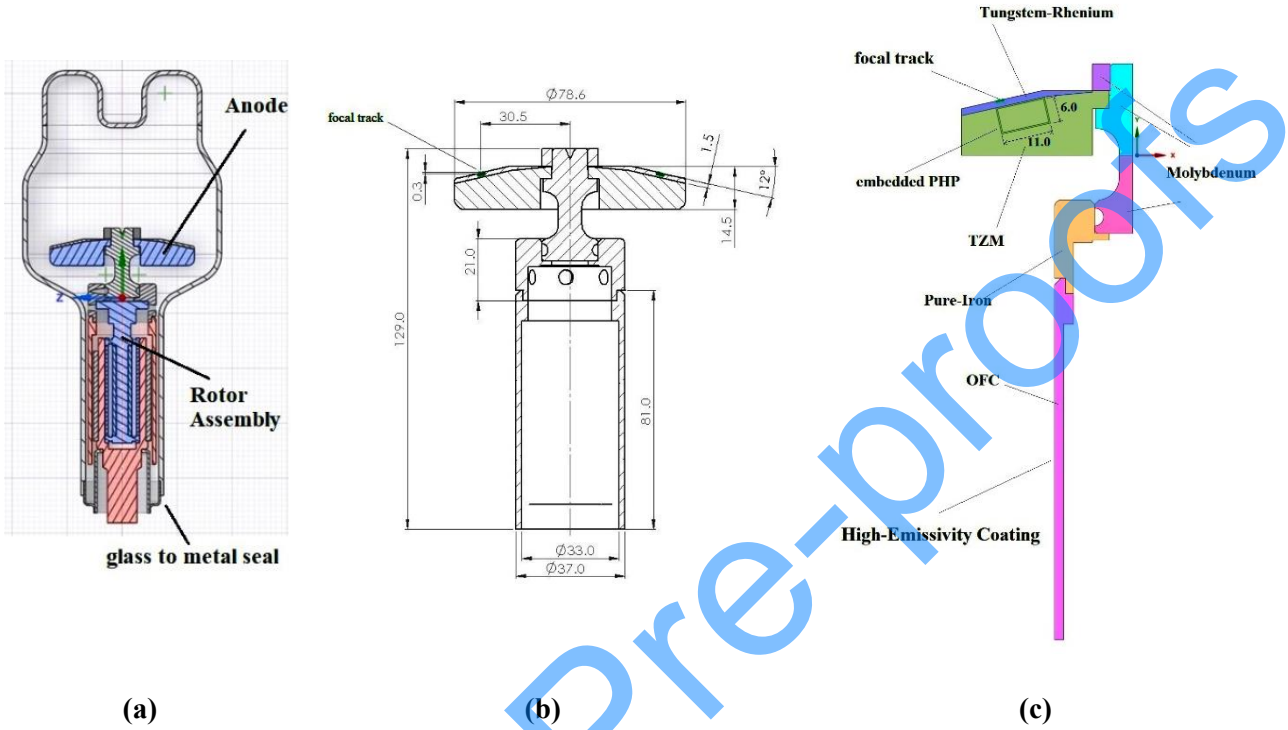

(a) **(b)** **(c)**

Fig 2. The RAD-14 rotating anode X-ray tube: (a) full 3D geometric representation, (b) simplified model with key dimensions, and (c) the final computational domain representing a 1.5 degree ($1/240^{th}$) periodic sector.

Although the catastrophic structural degradation of the anode typically occurs at approximately 2600 °C [3], a conservative thermal threshold of 2200 K is adopted in this study. This limit provides a high safety factor against premature failure and serves as a reliable benchmark to comparatively evaluate the cooling performance of the integrated RPHP.

The immense heat generated by the electron impact is initially absorbed by the anode, elevating the disk's temperature owing to its thermal capacity. Before this thermal energy can propagate deeply into the rotor assembly, it is predominantly dissipated to the surrounding environment (tube housing) via thermal radiation from both the anode disk and the Oxygen-Free Copper (OFC) component (as depicted in Fig. 2 (c)). To further enhance this radiative cooling, the external surface of the copper

block is typically treated with a specialized coating to maximize its thermal emissivity. Conversely, only a minimal fraction of the heat conducts through the rotor assembly towards the bearings and the glass-to-metal joint. This thermal isolation is an intentional design choice, achieved by reducing the heat transfer cross-sectional area and utilizing low-thermal-conductivity materials along the conduction path from the anode disk to the rotor, ultimately terminating at the glass-to-metal seal. Given that heat conduction to the rotor is negligible especially during the extremely short duration of a single-pulse operation the rotor assembly is excluded from the computational domain. Therefore, the numerical model focuses on the simplified solid structure shown in Fig. 2 (b). The core geometry comprises the rotating anode disk (made of Molybdenum alloy TZM) integrated with embedded square mini-channel (0.3 mm×0.3 mm), which form the RPHP network directly beneath the Tungsten-Rhenium focal track (the evaporator section).

To significantly reduce the enormous computational cost associated with transient 3D multiphase simulations, the computational domain is restricted to a 1/240 sector of the anode disk (Fig. 2 (c)). This structural simplification assumes an architecture of 240 equally spaced mini-heat pipes distributed azimuthally (θ-direction) around the disk. Symmetry boundary conditions are applied to the lateral faces of the sector to accurately replicate the continuous 360° nature of the physical disk.

2.2. Multiphase Flow and Fluid Domain Equations

The Volume of Fluid (VOF) model [31-33] was employed to model the two-phase flow behavior within the pulsating heat pipe. In this study, the VOF model is implemented within a rotating reference frame to account for centrifugal effects described as below [36].

2.2.1. Conservation Equations in a Rotating Reference Frame

In the rotating reference frame, the relative velocity ($\vec{v_r}$) is defined in relation to the absolute velocity ($\vec{v}$) and the whirl velocity ($\vec{\omega} \times \vec{r}$).

$$\vec{v_r} = \vec{v} - \vec{\omega} \times \vec{r} \quad (2)$$

where $\vec{\omega}$ is the angular velocity vector and $\vec{r}$ is the position vector from the origin of the rotation. The conservation equations for mass, momentum, and energy, adapted for the VOF model and rotating frame, are as follows:

$$\frac{\partial(\alpha_l)}{\partial t} + \nabla.(\alpha_l \vec{v}_r) = \frac{S_{\dot{m}.vl}}{\rho_l} \quad (3)$$

$$\frac{\partial \alpha_v}{\partial t} + \nabla \cdot (\alpha_v \vec{v}_r) = \frac{S_{\dot{m}.lv}}{\rho_v} \quad (4)$$

where α_l and α_v are the void fraction of liquid and vapor phases, ρ_l and ρ_v are their densities, and $S_{\dot{m}.vl}$ and $S_{\dot{m}.lv}$ are the mass transfer source terms from vapor to liquid phase and vice versa. The void fractions sum to unity ($\alpha_l + \alpha_v = 1$)

The mass source terms $S_{\dot{m}.vl}$ and $S_{\dot{m}.lv}$ are evaluated using the Lee evaporation–condensation model [37], as presented in Eq. (5):

$$S_{\dot{m}.vl} = \begin{cases} f \times \alpha_v \rho_v \dfrac{(T - T_{sat})}{T_{sat}} & T < T_{sat} \\ 0 & T > T_{sat} \end{cases}$$
$$S_{\dot{m}.lv} = \begin{cases} 0 & T < T_{sat} \\ f \times \alpha_v \rho_v \dfrac{(T - T_{sat})}{T_{sat}} & T > T_{sat} \end{cases} \quad (5)$$

The f coefficient represents the relaxation time. This coefficient is obtained from the Hertz–Knudsen formulation, derived based on kinetic theory and several assumptions were employed in its formulation, including a planar interface, a dispersed regime with constant droplet diameter, and a known value of the parameter β (accommodation coefficient [36]). Therefore, it should be determined empirically for each specific case study.

In the following sections, a parametric investigation of this coefficient is conducted. The VOF model computes a single shared velocity field, assuming negligible relative (slip) velocity

between the phases. This perfectly aligns with the characteristic liquid slug/vapor plug regime of PHPs, where vapor plugs occupy the entire channel cross-section rather than existing as dispersed or free-floating bubbles. Although a microscopic thin liquid film inherently exists at the walls, our macroscopic approach implicitly accounts for its effects within the mass transfer model. Consequently, the shared-velocity assumption is physically valid for this flow regime. The corresponding shared momentum equation is presented below.

$$\frac{\partial(\rho\overrightarrow{v_r})}{\partial t} + \nabla.(\rho\overrightarrow{v_r}\overrightarrow{v_r}) = -\nabla p + \nabla.\left[\mu\left(\nabla\overrightarrow{v_r} + \nabla\overrightarrow{v^T{}_r}\right)\right] + \rho\vec{g} - \rho[\vec{\omega}\times(\vec{\omega}\times\vec{r}) + 2\vec{\omega}\times\overrightarrow{v_r}] + \vec{F}_{vol} \quad (6)$$

where ρ is the mixture density, p is the pressure, μ is the mixture dynamic viscosity, $\vec{g}$ is the gravitational acceleration, $\rho[\omega\times(\omega\times r)]$ is the centrifugal force term, $\rho[2\omega\times v_r]$ represents the Coriolis force in the rotating frame, and $\vec{F}_{vol}$ includes other body forces like surface tension, modeled here via Continuum Surface Force model [38] as below:

$$F_s = \frac{\sigma\rho k\nabla\alpha_v}{\frac{1}{2}(\rho_v+\rho_l)} \quad (7)$$

In this equation, σ is the surface tension and k is the curvature of the liquid-vapor interface. The curvature of the liquid–vapor interface is obtained from the divergence of the gradient of the vapor volume fraction ($k = \nabla\cdot(\frac{\nabla\alpha_v}{|\nabla\alpha_v|})$) [36].

In the VOF model, the liquid and vapor phases are assumed to be in thermal equilibrium within each computational cell. Therefore, a single energy equation, utilizing averaged mixture properties, is solved for the fluid domain. This energy equation is expressed as below:

$$\frac{\partial(\rho E_r)}{\partial t} + \nabla\cdot[\rho\vec{v}_r H_r] = \nabla\cdot\left(k_{eff}\nabla T + \mu(\nabla\vec{v}_r)\cdot\vec{v}_r\right) + S_h \quad (8)$$

In this equation, k_{eff} denotes the overall conductive heat-transfer coefficient. The term S_h represents the energy transfer associated with mass transfer, which is evaluated using Eq. (9) [31].

$$S_h = -h_{lv} S_{\dot{m}.lv} = h_{lv} S_{\dot{m}.vl} \quad (9)$$

In this context, h_{lv} refers to the latent heat of phase change from liquid to vapor.

The relative internal energy of the fluid is denoted by E_r and can be obtained from Eq. (10). Similarly, the total relative enthalpy of the fluid, H_r, is determined using Eq. (11)

$$E_r = h - \frac{p}{\rho} + \frac{1}{2}(v_r^2 - u_r^2) \quad (10)$$

$$H_r = h + \frac{1}{2}(v_r^2 - u_r^2) \quad (11)$$

Here, the enthalpy h represents the sensible energy of the fluid, which is calculated using Eq. (12). The vector u_r denotes the rotational velocity ($\overrightarrow{u_r} = \vec{w} \times \vec{r}$)

$$h = \frac{\alpha_l \rho_l h_l + \alpha_v \rho_v h_v}{\alpha_l \rho_l + \alpha_v \rho_v} \quad (12)$$

In this relation, h_l and h_v represent the sensible energy of the liquid and vapor phases, respectively. These quantities are calculated from Eqs. (13) and (14), respectively. The zero-reference value of this energy is taken at the saturation condition.

$$h_l = C_{v.l}(T - T_{sat}) \quad (13)$$

$$h_v = C_{v.v}(T - T_{sat}) \quad (14)$$

The mixture fluid properties such as density (ρ), thermal conductivity (k_{eff}), and dynamic viscosity (μ) are calculated based on the void fraction of each phase using mixture rules:

$$\rho = \alpha_l \rho_l + \alpha_v \rho_v \quad (15)$$

$$k_{eff} = \alpha_l k_l + \alpha_v k_v \quad (16)$$

$$\mu = \alpha_l \mu_l + \alpha_v \mu_v \quad (17)$$

2.2.2. Turbulence Modeling

The $k - \omega$ SST (Shear Stress Transport) turbulence model is employed to resolve the flow dynamics. The primary rationale for selecting this model is its robustness in handling varying near-

wall conditions. Given that the present study evaluates various rotational speeds and mass transfer frequencies (f) utilizing a unified mesh scheme, the near-wall velocity gradients and local y^+ values can fluctuate significantly across different cases. The SST model addresses this through its advanced blending functions; these functions not only facilitate a seamless transition from the $k-\omega$ formulation in the near-wall region to the $k-\epsilon$ formulation in the central bulk flow of the 0.3 mm channel, but also when coupled with a y^+-insensitive wall treatment automatically adapts to the local mesh resolution. This dual blending capability ensures accurate boundary layer predictions regardless of the varying y^+ values, completely eliminating the need for mesh modifications for each specific operating condition.

2.3. Phase Change Kinetics

2.3.1. Lee Mass Transfer Model

In the present numerical framework, the evaporation and condensation frequency coefficient (f) in the Lee model was evaluated at three distinct values (0.1, 10, and 1000 s^{-1}), with 1000 s^{-1} ultimately selected for the liquid lithium domain. While the default value is often 0.1 s^{-1} for conventional fluids, practical engineering applications frequently require values up to 1000 s^{-1} to accurately capture rapid phase change dynamics [36]. Furthermore, comprehensive assessments [39, 40] demonstrate that this empirical factor can physically range from 0.01 to 10^7 s^{-1} depending on the thermophysical regime. Based on the exact Lee model formulation derived from the Hertz-Knudsen equation ($f = \frac{6}{d}\beta\sqrt{\frac{M}{2\pi RT_{sat}}}L(\frac{\rho_l}{\rho_l-\rho_g})$) [36], the application of f=1000 s^{-1} for the Lithium-filled Rotating Pulsating Heat Pipe (RPHP) is fundamentally justified. The accommodation coefficient, β, which is often low for polar fluids like water due to significant interfacial thermal resistance, approaches its theoretical kinetic limit ($\beta\rightarrow1$) for liquid lithium in this application due to a synergy of factors:

(1) Impact of Thermophysical Properties and Geometric Scale: Excluding the accommodation

coefficient (β), the theoretical phase change frequency of lithium is orders of magnitude greater than that of water, driven by both its intrinsic properties and the geometric scale of the application. For our validation case of water at 96 ℃ (d=4.5 mm), the theoretical frequency evaluates to $f_{water}\approx 2.8\times10^{6}\ \beta$. In stark contrast, for liquid lithium evaluated at 1300 K within the RPHP mini-channel (d=0.3 mm), the high latent heat yields a massively higher phase change frequency ($f_{Lithium}\approx 1.3\times10^{8}\ \beta$).

(2) Extreme Centrifugal Forces and Thin-Film Formation: High rotational speeds (2850–10,000 rpm) generate immense centrifugal acceleration (up to ~ 3200g). This compresses the liquid lithium against the channel walls, creating an ultra-thin film. This morphological change is critical because it directly mitigates interfacial thermal resistance, a primary factor that lowers β in conventional systems. By minimizing the conduction path from the wall to the liquid-vapor interface, the heat required for vaporization is supplied instantaneously, preventing the local temperature drop that would otherwise hinder phase change kinetics. Consequently, the process is no longer limited by thermal transport, allowing β to approach its theoretical kinetic limit of unity.

(3) Superior Thermal Conductivity: Liquid lithium possesses exceptionally high thermal conductivity (k≈60 W/m·K), approximately 100 times that of water. This property, combined with the ultra-thin film created by rotation, virtually eliminates interfacial thermal resistance. Heat required for vaporization is supplied instantaneously to the interface, preventing the local temperature drop that typically lowers the effective β in conventional fluids.

(4) Engineered Surface Topography: The internal walls of the RPHP are not treated as ideal smooth surfaces. Instead, they are deliberately engineered with a specific micro-scale topography, including fabricated cavities. This is not incidental roughness but a targeted design feature intended to maximize phase change efficiency. By creating these surfaces, we drastically increase the density of active nucleation sites, promote capillary-assisted liquid spreading, and enhance the effective interfacial area. This engineered approach accelerates evaporation kinetics far beyond what is possible on a smooth, flat interface.

Considering the aforementioned points, it is evident that the phase change process of liquid lithium in this system operates close to its ideal kinetic limit. With β approaching unity, the theoretical coefficient can practically exceed 10^7 s^{-1}. Therefore, the utilized value of f=1000 s^{-1} is a highly conservative, physically robust estimate that ensures numerical stability while adequately resolving the rapid evaporation kinetics of lithium.

2.3.2. Pressure-Dependent Saturation Temperature

To accurately model the phase change dynamics, strict thermodynamic consistency must be maintained between the initial state and the transient evolution of the system. The simulation initializes at a pre-heated state of $T_{init} = 1300$ K. Accordingly, the initial internal pressure (P_{init}) is strictly set to approximately 6586 Pa, which precisely corresponds to the equilibrium vapor pressure of lithium at this initial temperature.

During the transient simulation, the local pressure field evolves due to heat addition, phase change, and rotational forces. The local pressure of the vapor phase is dynamically computed using the Peng-Robinson Equation of State (PR-EOS), which accurately captures the compressibility and real-gas behavior of lithium vapor under these operating conditions. The choice of PR-EOS provides an optimal balance, ensuring sufficient thermodynamic accuracy to capture the high sensitivity of saturation temperature to pressure, while avoiding the severe numerical divergence often caused by integrating custom equations of state (via UDFs) with the highly non-linear VOF model under extreme body forces.

The PR-EOS is formulated as follows [36]:

$$p = \frac{RT}{v-b} - \frac{a(T)}{v(v+b)+b(v-b)} \tag{18}$$

where p is the pressure, T is the absolute temperature, v is the molar volume, and R is the universal gas constant. The substance-specific parameters $a(T)$ and b are determined from the critical

properties (T_c, p_c) and the acentric factor (ω):

$$a(T) = 0.45724\frac{R^2T_c^2}{p_c}\alpha(T) \tag{19}$$

$$b = 0.07780\frac{RT_c}{p_c} \tag{20}$$

The temperature dependency of the attraction parameter is captured by $a(T)$, which is a function of the acentric factor ω:

$$\alpha(T) = \left[1 + k\left(1 - \sqrt{\frac{T}{T_c}}\right)\right]^2 \tag{21}$$

$$k = 0.37464 + 1.54226\omega - 0.26992\omega^2 \tag{22}$$

The required lithium properties for this equation of state are specified as follows [41]: critical temperature T_c=3220 K, critical pressure p_c=67×10^6 Pa, molecular weight M=6.9 g/mol, and an acentric factor of ω=−0.045. Simultaneously, severe centrifugal acceleration in the high-speed RPHP induces substantial hydrostatic pressure gradients ($\Delta P \propto \rho_l r^2 w^2$) within the liquid phase. To determine the accurate onset of boiling and condensation under these fluctuating pressure fields, the model dynamically couples the local absolute pressure to the phase-change temperature. This is achieved by inputting the dataset of lithium's saturation temperature as a function of saturation pressure (T_{sat} vs. P_{sat}) [41] into the solver as a piecewise-linear profile. At each computational cell and time step, the solver utilizes the locally calculated pressure (derived from the PR-EOS and momentum equations) to interpolate this dataset, yielding the exact local boiling temperature, $T_{sat}(P_{local})$. This rigorous coupling ensures that the boiling point shifts physically in response to both the centrifugal hydrostatic penalty and the transient vapor pressure generation.

2.4. Solid Domain and Interfacial Conditions

2.4.1. Heat Conduction in Solid Regions

The transient temperature distribution within the solid components of the anode (i.e., the TZM

disk and the tungsten-rhenium focal track) is governed by the three-dimensional unsteady heat conduction equation. The energy equation is expressed as [42]:

$$\rho_s Cp_s \frac{\partial T_s}{\partial t} = \nabla.(k_s \nabla T_s) \quad (23)$$

where ρ_s Cp_s and k_s represent the density, specific heat capacity, and thermal conductivity of the respective solid material, and T_s is the solid temperature.

The primary thermal load from the electron beam is applied as a highly concentrated, transient heat flux boundary condition at the focal track surface:

$$-k_s(\nabla T_s.\vec{n}) = q''_{eb}(r) \quad (24)$$

where $\vec{n}$ is the unit normal vector to the target surface, and $q''_{eb}(r)$ is the spatial distribution of the electron beam heat flux.

2.4.2. Conjugate Heat Transfer (CHT) and Interface Coupling

To accurately model the heat flow throughout the entire computational domain, specific coupling conditions are enforced at the interfaces between different materials and phases. Perfect thermal contact (zero thermal contact resistance) is assumed at the interfaces between the different solid domains of the anode (i.e., Tungsten and TZM). This assumption is physically justified because, in the practical manufacturing of high-performance rotating X-ray anodes, these distinct material layers are cohesively bonded using techniques such as powder metallurgy, high-temperature vacuum brazing, or chemical vapor deposition (CVD) to endure extreme centrifugal forces and thermal stresses.

Solid-Solid Interface: At the interface between two different solid materials (e.g., the tungsten-rhenium focal track and the TZM anode disk), the continuity of both temperature and heat flux is strictly maintained:

$$T_{s1} = T_{s2} \quad (25)$$

$$-k_{s1}(\nabla T_{s1}.\vec{n}_{int}) = -k_{s2}(\nabla T_{s2}.\vec{n}_{int}) \quad (26)$$

where subscripts $s1$ and $s2$ denote the two adjacent solid materials, and $\vec{n}_{int}$ is the normal vector at their common interface.

Solid-Fluid Interface (Conjugate Heat Transfer): To couple the solid domain with the multiphase working fluid (lithium) inside the RPHP channels, a Conjugate Heat Transfer (CHT) approach is utilized.

A no-slip boundary condition is applied at the fluid-solid interface, mandating that the fluid velocity at the wall is equal to the velocity of the rotating solid wall. For the thermal coupling, the interface requires the continuity of temperature and conductive heat flux, similar to the solid-solid boundary:

$$T_s = T_f \quad (27)$$

$$-k_{s1}(\nabla T_s.\vec{n}_{int}) = -k_{eff}(\nabla T_f.\vec{n}_{int}) \quad (28)$$

2.5. Boundary Conditions, Initial Conditions, and Material Properties

The domain reproduces the multi-material construction of the anode: W-Re, Molybdenum, TZM, Pure-Iron, and OFC.

2.5.1. Boundary and Initial Conditions

As illustrated in Fig. 3, the computational domain is subjected to specific thermal and rotational boundary conditions to simulate operational exposure. the complete set of applied initial and boundary conditions, including surface emissivities for radiative cooling, are summarized in Table 1.

Table 1. Summary of initial and boundary conditions applied to the numerical domain.

Domain	Condition Type	Value / Description
Focal Track	Heat Flux	Equivalent to a 20-kW heat input
External Surfaces	Radiation to Environment 300 K	Emissivities (ϵ): W-Re = 0.3, TZM = 0.2, OFC = 0.9, Fe = 0.05, Mo = 0.1
Lateral Sector Surfaces	Boundary Condition	Symmetry ($\frac{\partial T}{\partial n} = 0$)
Anode Disk	Frame motion	Rotation in the positive y-direction at four angular velocities (2850, 3450, 8500, and 10000 rpm)
Fluid and solid	Initial Temperature	1300 K (representing sequential scans)
Fluid	Initial Pressure	6586 Pa (Saturation pressure at 1300 K)
Fluid	Initial Liquid Filling Ratio	0.78

The lateral surfaces of the simulated 1.5° sector are modeled using symmetry boundary conditions. While rotational periodic boundaries are generally standard for continuous rotating domains, the specific configuration of our model lacks embedded pulsating heat pipe (PHP) channels in the azimuthal (θ) direction. Consequently, temperature variations and gradients in the θ direction near the lateral boundaries are practically negligible. Under these specific geometrical constraints, the computationally simpler symmetry boundary condition is mathematically adequate and yields thermal results equivalent to periodic conditions without compromising accuracy.

Regarding the initial thermal state, the entire computational domain is set to an initial temperature of 1300 K. In practical operation, X-ray tubes are typically evaluated under sequential loading conditions rather than an idealized cold start. Rating charts indicate that the maximum applicable power depends on thermal history: a cold tube permits the highest instantaneous load, whereas a pre-heated tube, consistent with realistic disk temperatures, operates at a reduced allowable power. Therefore, 1300 K represents a physically plausible operating scenario for sequential scans. Consequently, the initial internal pressure of the RPHP is set to 6586 Pa, corresponding to the saturation pressure of lithium at this operational baseline temperature.

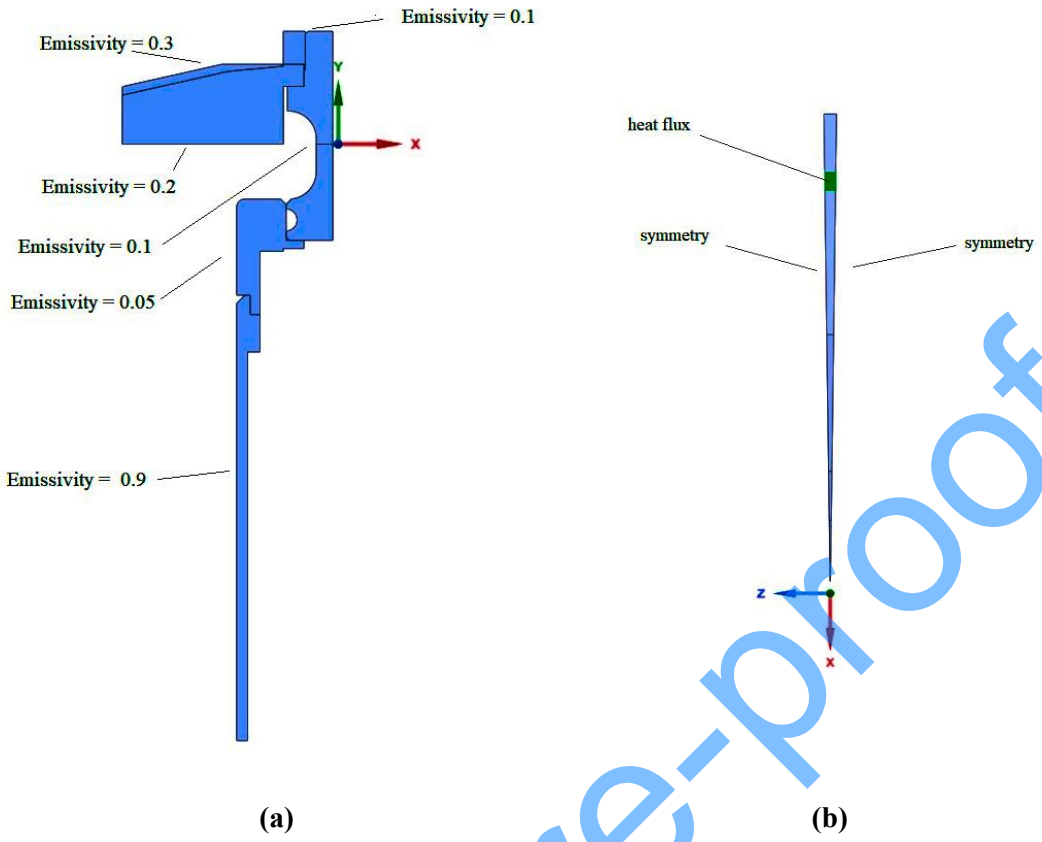

(a) **(b)**

Fig 3. Boundary conditions applied to the computational domain: (a) distribution of surface emissivity coefficients on the exterior boundaries, and (b) location of the applied heat flux and symmetry planes on the 1.5° sector model.

PHP Geometry: The embedded pulsating heat pipe (PHP) is machined beneath the Tungsten–Rhenium layer, fully located within the TZM region. The channel cross-section is square with dimensions of 0.3 mm × 0.3 mm. The PHP geometry has an in-plane length and width of 6 mm × 11 mm, as indicated in Fig. 2 (c). Radially, its farthest point lies at 31.5 mm from the y-axis. In the circumferential (θ) direction, the PHP is positioned at the center of the simulated 1.5° sector. The adoption of a rectangular loop geometry for the internal channels is primarily driven by manufacturability constraints. Given the extreme hardness of the TZM alloy used in the anode, creating deep, internal curved channels (e.g., elliptical loops) is highly impractical. Standard precise machining methods for such refractory metals, such as Spark Electrical Discharge Machining, naturally yield straight paths. Thus, evaluating the PHP under these practical, worst-case

manufacturing constraints ensures that the proposed cooling design is both thermally effective and industrially feasible.

2.5.2. Thermophysical Properties of Materials

Although the target surface temperature experiences a drastic increase from 1300 K to approximately 2200 K during the operation, the temperature variation within the heat pipe itself is significantly restricted, ranging only from 1300 K to about 1760 K. This bounded temperature range is a direct result of the effective temperature-regulating mechanism provided by the liquid metal phase change. Consequently, to facilitate numerical convergence and maintain a reasonable computational cost in the model, the primary thermophysical properties of lithium including density, specific heat capacity, thermal conductivity, dynamic viscosity (for both liquid and vapor phases), latent heat, and surface tension were assumed to be constant and evaluated at the reference temperature of 1300 K.

Instead, the primary modeling focus was directed toward the pressure dependence of the saturation temperature ($T_s(p_{local})$). This is a critical physical aspect of the present study, as the local internal pressure of the heat pipe undergoes substantial spatial and temporal variations due to the immense centrifugal forces at varying rotational speeds and the transient heating process. The thermophysical properties utilized in the present numerical simulation for lithium and TZM are summarized in Tables 2 and 3, respectively. The temperature-dependent properties of other solids, including tungsten-rhenium, copper, iron, and molybdenum, were obtained from Incropera [42].

Table 2. thermophysical properties of lithium [41].

h_{lv} (kJ/kg)	ρ_l (kg/m^3)	μ_l (N.s/m^2)	μ_v (N.s/m^2)	k_l (W/mK)	k_v (W/mK)	σ (N/M)	cp_l (J/kgK)	cp_v (J/kgK)
20380	432	0.00019	1.2×10^{-5}	62	0.15	0.28	4160	532

Table 3. thermophysical properties of TZM [43].

Temperature (K)	ρ (kg/m^3)	*Cp* (J/kg.K)	*k* (W/m.K)
300	10200	226	123
1673	10200	356	89
2273	10200	410	77

2.6. Summary of Physical Parameters and Variables

Several heat pipe parameters—such as the type of working fluid, the geometric architecture of the channels within the anode disk (including length, width, and arrangement), and the liquid filling ratio—significantly influence the thermal performance of the X-ray tube and could potentially be subjected to parametric studies. However, in the present study, these parameters were strategically optimized and fixed based on specific engineering rationales:

Working Fluid: For the target high-temperature range, silver, sodium, and lithium are viable candidates. Lithium was specifically selected as the optimal choice due to its appropriate vapor pressure within the anode's operating regime, exceptionally high latent heat, and high surface tension, which allows it to maintain equilibrium against extreme centrifugal forces. Additionally, its low-density results in lower hydrostatic pressure under rapid rotation, thereby minimizing nucleation delay at high rotational speeds.

Geometric Architecture: The channel cross-sectional dimensions (0.3×0.3 mm) are strictly governed by Equation (1) to satisfy the necessary capillary limit, leaving minimal design flexibility for this specific parameter. However, the length, width, and overall structural layout of the channels were deliberately tailored by the author to maximize the utilization of the anode disk's thermal capacity.

Filling Ratio: A relatively high initial liquid filling ratio was adopted to effectively mitigate the risk of dry-out phenomena under severe thermal loads.

With these foundational design choices established, the physical framework of the problem prior to the mesh independence analysis is explicitly categorized into independent (influencing) and dependent (influenced) parameters to clarify the numerical inputs and expected outcomes

Independent Parameters: Geometric Parameters: Dimensions of the final computational domain, including the features illustrated in Fig. 2(b, c) and the supplementary geometrical data detailed in Section 2.5.1.

Operational and Boundary Conditions: Thermal load at the focal track, anode rotational speed, ambient temperature, radiative cooling emissivity, and initial liquid filling ratio.

Thermophysical and Multiphase Properties: Solid material properties, PR-EOS for lithium vapor, latent heat of vaporization, surface tension, and phase change parameters (specifically, the evaporation and condensation frequencies used in the Lee model [36]).

Dependent Parameters:

Primary Field Variables: Pressure field, fluid velocity vector, temperature field, and volume fractions of liquid and vapor phases and interphase mass transfer rate.

Extracted Performance Metrics: Since the primary objective of this study is to determine the maximum allowable exposure time before the average focal track reaches the critical temperature limit of 2200 K, the average temperature of the focal track (T_{avg}) is selected as the key index for the mesh independence study.

3. Numerical Validation and Mesh Independence

3.1. Numerical Validation

To establish the validity of the numerical framework, a benchmark study was conducted. A central feature of the present simulation is the coupling of the Volume of Fluid (VOF) method with a pressure-dependent saturation temperature formulation ($T_{sat}(p)$) within the Lee phase-change model. Therefore, a primary objective of this validation was to specifically verify the model's

accuracy in predicting the transient pressure dynamics that govern the boiling process. For this purpose, the experimental investigation by Yang *et al.* [44] on a stationary Pulsating Heat Pipe (PHP) was selected, as it provides the necessary experimental pressure data for a direct comparison.

The experimental setup from the reference study is shown in Fig. 4. A numerical simulation was performed replicating this geometry. In their setup, a copper tube with an inner diameter of 4.5 mm and an outer diameter of 6.2 mm was utilized, and water was selected as the working fluid.

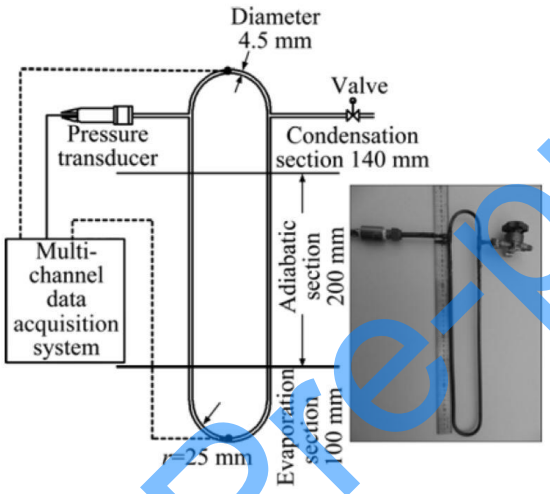

Fig 4. Schematic setup of validation model [44].

Fig. 5 presents a comparison between the transient internal pressure predicted by our numerical model and the experimental measurements. The simulation results, obtained with a mesh size of 0.1 mm and an evaporation-condensation coefficient of 0.1, demonstrate excellent agreement with the experimental data. The numerical prediction (Fig. 5(a)) faithfully reproduces all three experimental regimes (Fig. 5(b)): the initial gradual pressure rise, chaotic pulsations due to slug formation, and the quasi-steady plateau (~70 kPa) after approximately 40 s. It should be noted that due to the inherently chaotic and stochastic nature of two-phase flow in PHPs, exact point-to-point temporal matching between numerical and experimental pressures is not feasible. The slight deviations in the transient phase and initial pressure are attributed to idealized conditions in the CFD model and experimental

uncertainties; however, the excellent agreement in the fluctuation trend and maximum steady-state pressure (~76 kPa vs ~72 kPa) confirms the reliability of the present numerical model.

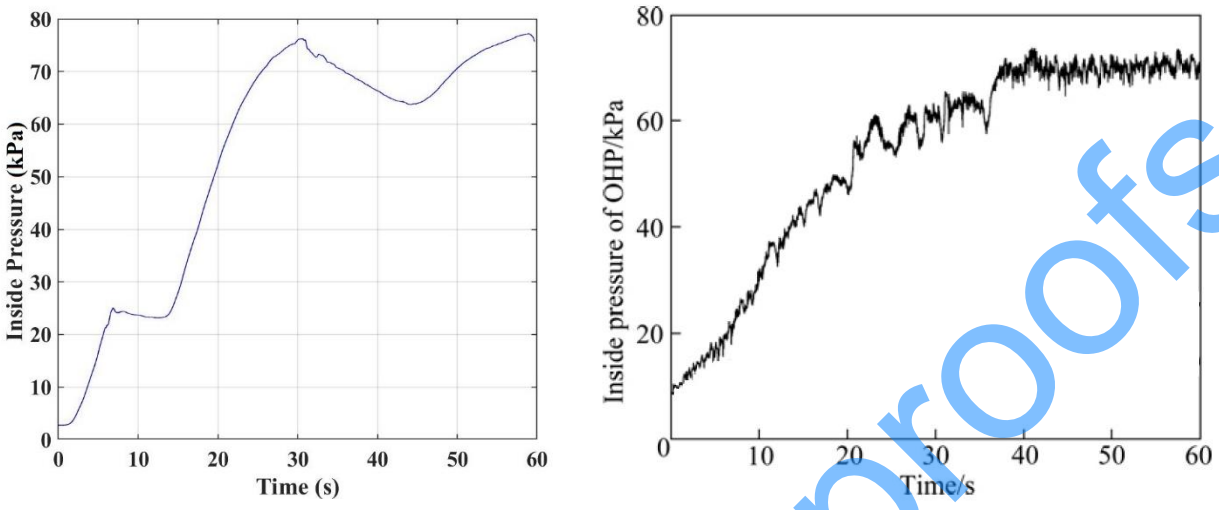

(a) **(b)**

Fig 5. Comparison of the heat pipe internal pressure variations over time: (a) present numerical simulation, (b) experimental results [44].

This strong correlation validates the fundamental accuracy of the implemented two-phase flow and heat transfer physics. However, it is crucial to highlight the distinctions between the validation case and the primary focus of the present research. Table 4 outlines these key differences. While the validation study confirms the solver's core capabilities for modeling boiling and condensation, our work extends this validated framework to a significantly more complex and extreme environment. The present study introduces ultra-high-speed rotation, which generates massive body forces (centrifugal and Coriolis) entirely absent in the stationary PHP benchmark. Furthermore, the application involves extreme high-temperature conditions and utilizes a liquid metal (lithium) as the working fluid, requiring the model to capture complex two-phase hydrodynamics and thermal phenomena within the X-ray anode.

Table 4. Comparison between the Validation Study and the Present Work.

Feature	Validation study [44]	Present work
Geometry	Simple pulsating heat pipe (PHP)	RPHP within an x-ray anode
Working fluid	Conventional fluid (water)	Liquid metal (lithium)
Operating temperature	Low to moderate	Extremely high
Primary physics	Stationary two-phase flow	Rotating two phase flow
Dominant forces	Gravity, Surface Tension	Centrifugal, Coriolis, Surface Tension
Objective	Characterize PHP performance	Enhance anode thermal performance

3.2. Mesh Independence Study

Having successfully validated the numerical framework against experimental data in the preceding section, the focus now shifts to the primary case study: the rotating anode X-ray tube. Before proceeding with the main parametric investigations, a mesh independence study was conducted specifically for this geometry to ensure the reliability of the numerical results.

To evaluate mesh independence, three polyhedral grids: coarse (0.075 mm), medium (0.045 mm), and fine (0.03 mm) were generated for the fluid region using Fluent Meshing (exemplified in Fig. 6), with the surrounding solid domain meshed using a growth rate of 1.2.

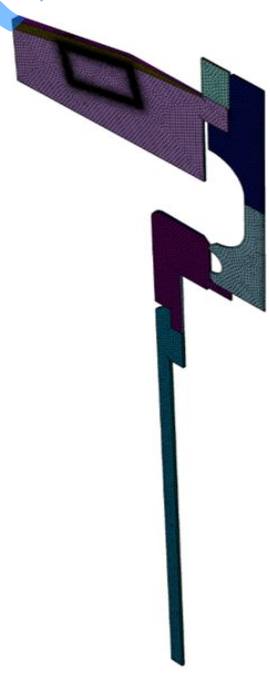

Fig 6. The polyhedral computational mesh used for the numerical simulation.

As shown in Fig. 7, evaluating the average focal track temperature at t=0.561 s reveals close convergence between the medium (2176.8 K) and fine (2184.6 K) grids. Because the relative deviation is merely 0.35%, the medium mesh was adopted for all simulations to maintain high accuracy while reducing computational cost.

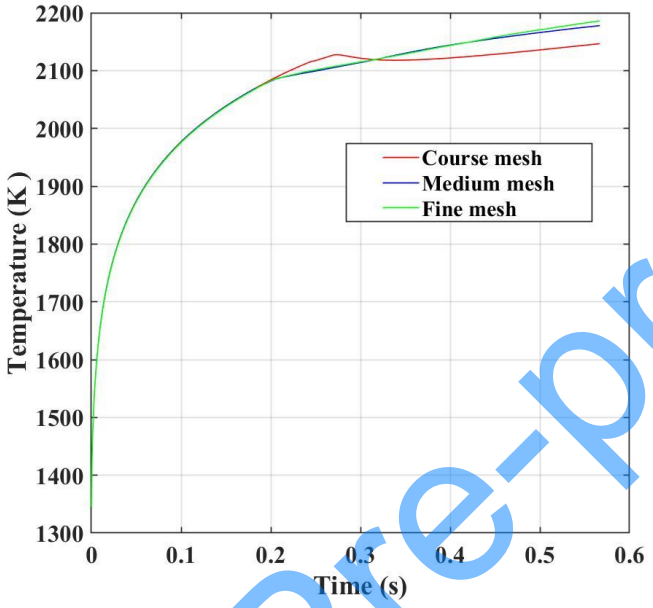

Fig 7. Effect of mesh size on average focal track temperature (mesh study).

4. Results and Discussion

4.1. Effect of Mass Transfer Frequency on RPHP performance

The accuracy of the Lee phase-change model heavily relies on the empirical mass transfer frequency (relaxation time), denoted as f. While theoretical expectations suggest that the mass transfer frequency for liquid metals like lithium significantly exceeds 1000 s^{-1}, its exact value in this specific extreme environment remains uncertain. To ensure a conservative prediction of the cooling capacity, an upper limit of 1000 s^{-1} was adopted. Furthermore, a parametric study was performed including artificially lower frequencies (f=0.1 and 10 s^{-1}) alongside f=1000 s^{-1} at a rotational speed of 8500 rpm. This analysis aims to evaluate the system's thermal response if unforeseen factors—such as impurities, non-condensable gases, or any other restrictions—were to severely degrade the effective

evaporation and condensation rates. The thermal response was compared against a baseline solid target (without the embedded heat pipe). Fig. 8 illustrates the mean temperature at the focal track for the different cases, with the resulting allowable exposure times summarized in Fig. 9.

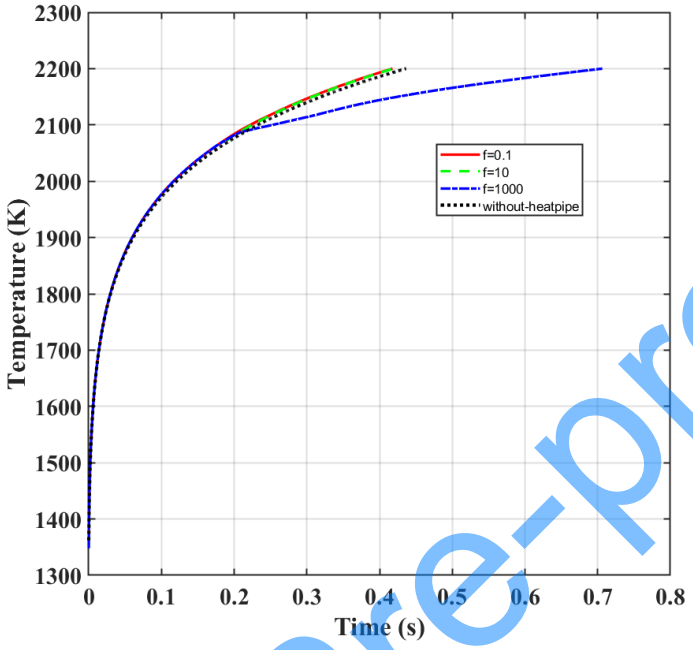

Fig 8. Effect of evaporation-condensation frequency (*f*) on the maximum allowable exposure time, limited by an average focal track temperature of 2200 K at 8500 rpm.

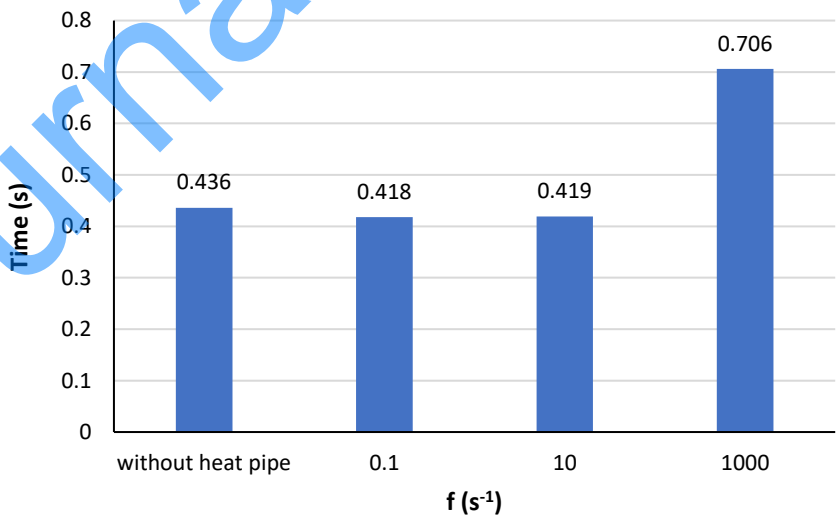

Fig 9. Allowable exposure time for the system without a heat pipe and with 7za heat pipe at different *f* at 8500 rpm.

A critical physical phenomenon is observed: for low evaporation-condensation frequencies (f=0.1 and 10 s^{-1}), the RPHP performs poorly. The allowable exposure times in these cases are 0.418 s and 0.419 s, respectively. Counter-intuitively, these values are approximately 4% shorter than the 0.436 s achieved by the baseline target without a heat pipe, indicating a detrimental effect. In stark contrast, a high frequency of f=1000 s^{-1} enables effective thermal management, extending the exposure time to 0.706 s, a 62% improvement over the baseline.

This adverse effect is physically sound. At low mass transfer frequencies, the phase-change process is highly suppressed. This thermohydraulic behavior is vividly substantiated by the vapor volume fraction distributions (Fig. 10 (a)). At f=0.1 and 10 s^{-1}, phase change is severely restricted, resulting in sparsely distributed, isolated vapor bubbles with negligible volumetric presence. The micro-channels remain predominantly filled with liquid lithium (vapor fraction ≈0). Since liquid lithium possesses a lower thermal conductivity compared to the solid TZM alloy it replaces, the inactive RPHP acts as an internal thermal resistance, governed strictly by weaker thermal conduction.

Conversely, setting f=1000 s^{-1} accurately captures the vigorous micro-scale boiling expected under severe centrifugal forces. As observed in the vapor volume fraction contour for f=1000 s^{-1}, rapid and continuous nucleation occurs. The intense vapor generation leads to rapid bubble coalescence, forming extensive vapor slugs and transitioning the system into an annular-like flow regime along the channel boundaries.

As shown in the relative velocity magnitude contours (Fig. 10 (b)), while the suppressed boiling at low frequencies results in low fluid motion (V_{max}≈1.01−1.33 m/s), the continuous vapor generation at f=1000 s^{-1} drives a robust circulation of the working fluid with velocities surging up to 8.49 m/s.

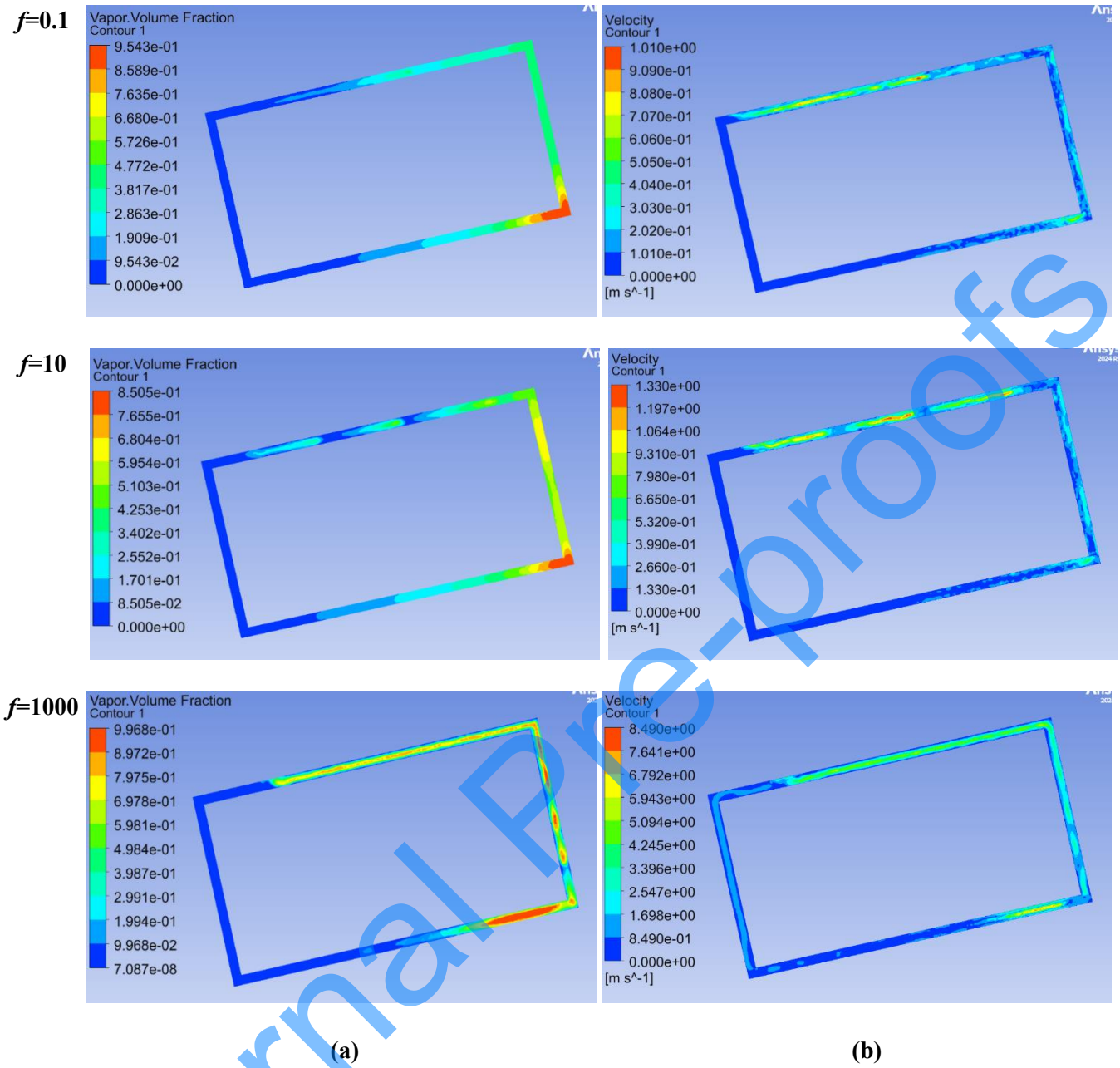

Fig 10. Effect of lee mass transfer frequency on volume fraction (a) and velocity contours (b) at 0.5 s.

This combined effect of an annular-like vapor flow and high-velocity liquid circulation signifies the successful activation of the RPHP. The dominant heat transfer mechanism successfully transitions from poor liquid conduction to highly efficient two-phase flow boiling and latent heat and sensible heat transport. Consequently, the focal track temperature is drastically mitigated. Based on this comprehensive thermohydraulic evidence, f=1000 s^{-1} was established as the physically consistent, yet fundamentally conservative, parameter for the active RPHP in all subsequent simulations.

4.2. Effect of rotational speed on RPHP performance

The primary metric for evaluating the thermal performance of the RPHP-integrated anode is the maximum allowable exposure time before the average focal track temperature reaches a predefined critical limit of 2200 K. Since commercial rotating anode X-ray tubes typically operate at distinct, predefined rotational speeds, four standard operational speeds—namely 2850, 3450, 8500, and 10000 rpm—were selected for the present analysis. The investigation into the effect of these rotational speeds reveals a non-monotonic relationship with the allowable exposure time, as illustrated by the transient temperature profiles in Fig. 11 and summarized quantitatively in Fig. 12.

The results clearly demonstrate the efficacy of the RPHP. The baseline anode without an RPHP reaches the critical temperature in just 0.436 s. The integration of the RPHP extends this duration across all tested speeds. A progressive enhancement is observed as the rotational speed increases from 2850 rpm (0.528 s) to 3450 rpm (0.589 s), culminating in an optimal performance at 8500 rpm. At this speed, the focal track can sustain the thermal load for a maximum of 0.706 s, representing a significant 62% improvement in exposure time compared to the baseline.

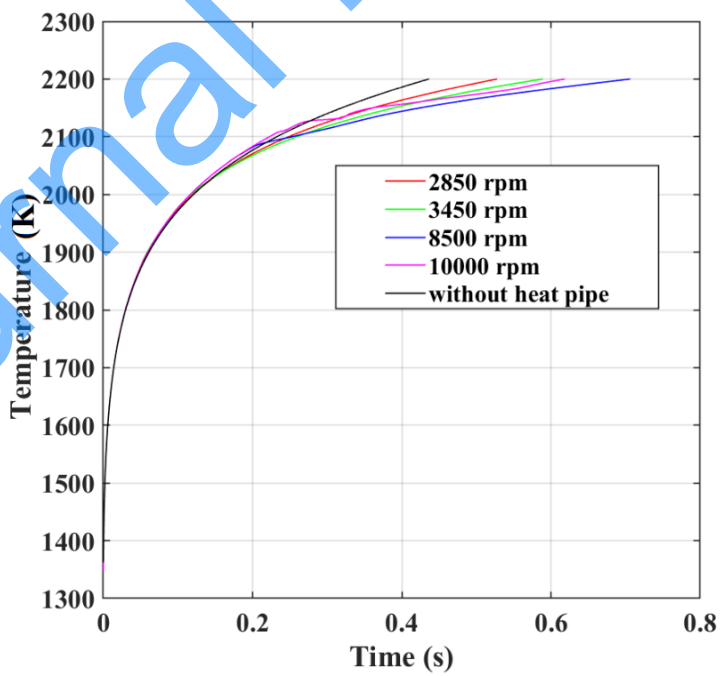

Fig 11. Effect of rotational speed on the average focal track temperature evolution.

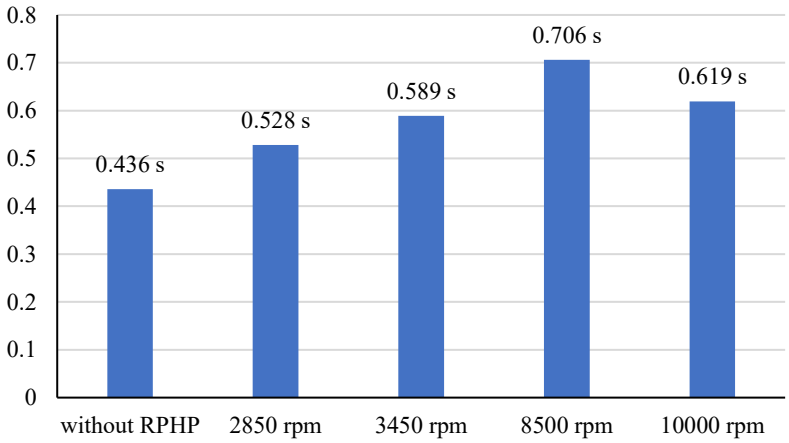

Fig 12. Allowable exposure time for the system without a heat pipe and with a heat pipe at different rotational speed.

However, this trend reverses at higher speeds. At 10000 rpm, a degradation in thermal performance is observed, with the allowable exposure time decreasing to 0.619 s. While still a substantial improvement over the baseline, this is a 12% reduction from the peak performance achieved at 8500 rpm. The following analysis of the detailed velocity and pressure fields (as shown in Fig. 13 and Fig. 14) delves into the competing physical mechanisms responsible for this performance trade-off and the existence of an optimal rotational speed.

Centrifugal acceleration plays a dual role in the thermal-hydraulic performance of the RPHP . Fig. 13 illustrates the velocity contours of the liquid-vapor mixture at t=0.5 s for different rotational speeds ranging from 2850 to 10000 rpm. A monotonic increase in the maximum fluid velocity is clearly observed. As the rotational speed increases from 2850 rpm to 10000 rpm, the maximum circulation velocity accelerates significantly from 4.33 m/s to 11.6 m/s. This flow acceleration is the result of a dual pumping mechanism within the closed-loop geometry. On one hand, the intensified centrifugal acceleration at higher speeds strongly propels the liquid condensate back from the condenser to the evaporator. On the other hand, this robust centrifugal return flow is coupled with the pressure-driven pumping action caused by continuous bubble generation and expansion in the evaporator, resulting in a significantly higher internal circulation velocity.

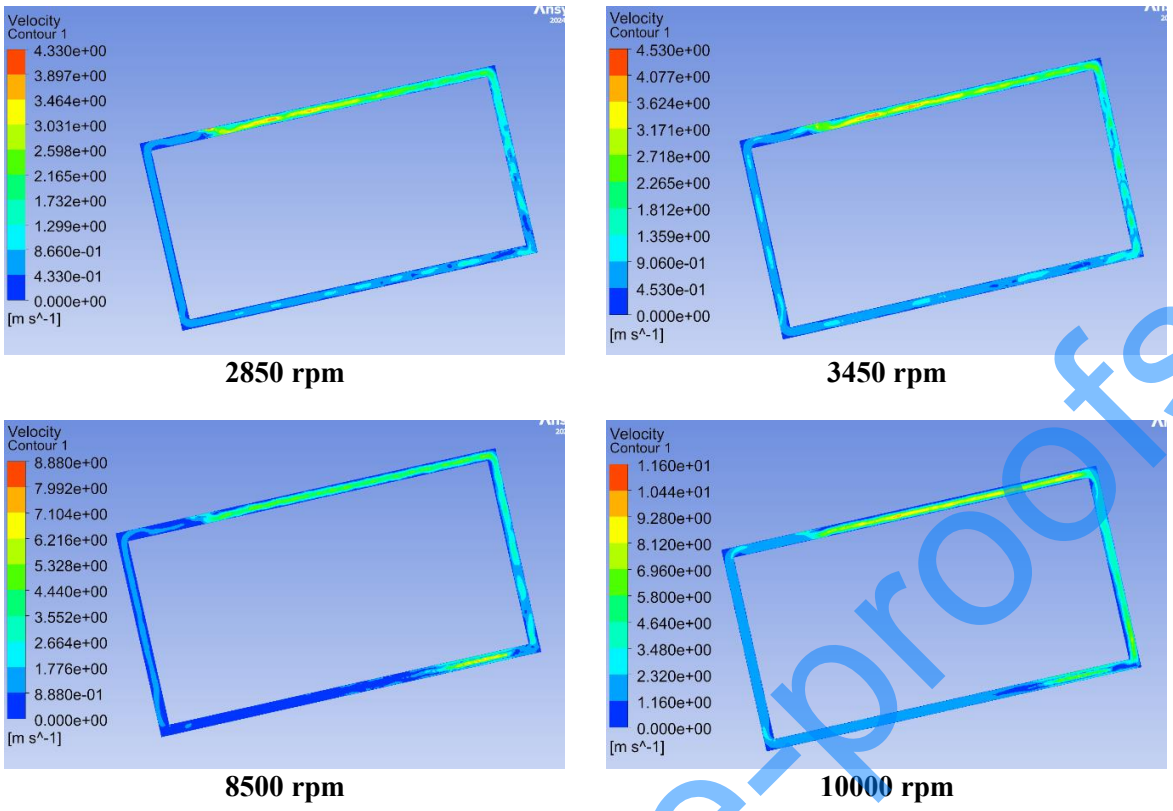

Fig. 13. Velocity contours illustrating the effect of rotational speed on the internal fluid circulation at t=0.5 s.

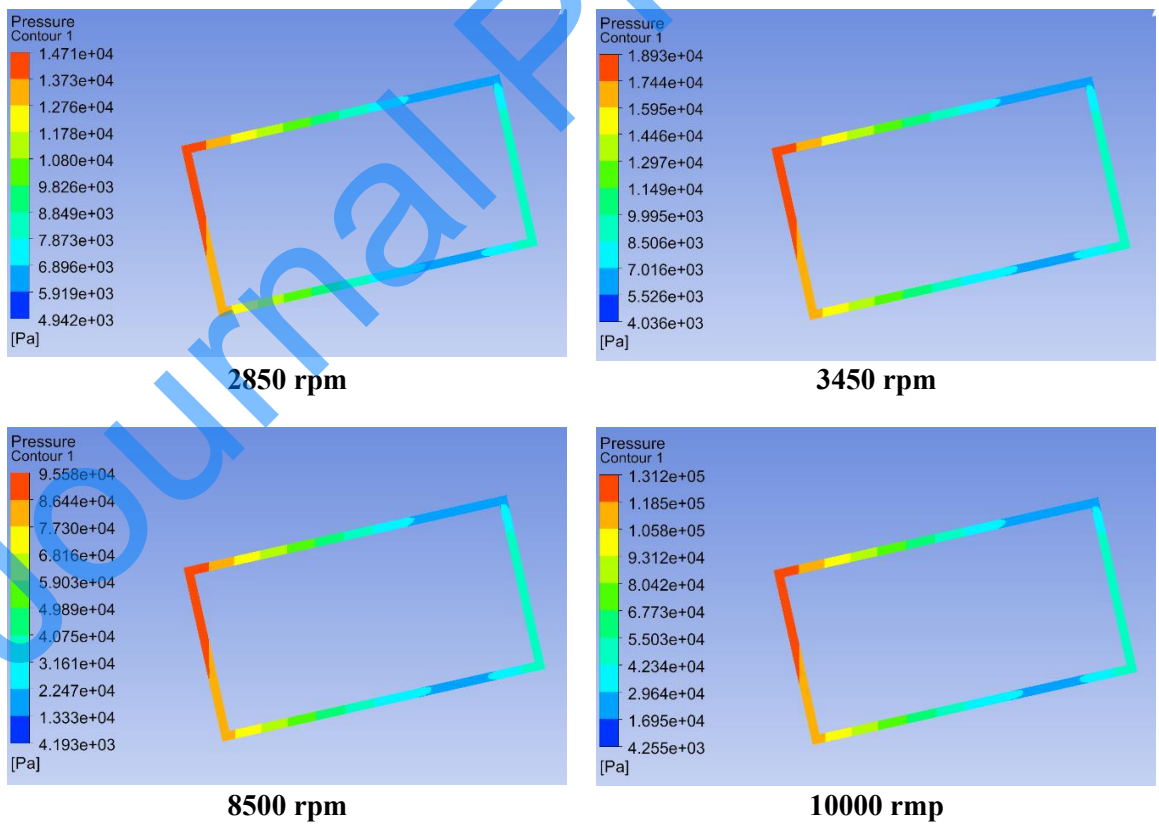

Fig. 14. Pressure contours illustrating the effect of rotational speed on the hydrostatic pressure build-up at early stages (t=0.01 s).

Centrifugal acceleration plays a dual role in the thermal-hydraulic performance of the RPHP . Fig. 13 illustrates the velocity contours of the liquid-vapor mixture at t=0.5 s for different rotational speeds ranging from 2850 to 10000 rpm. A monotonic increase in the maximum fluid velocity is clearly observed. As the rotational speed increases from 2850 rpm to 10000 rpm, the maximum circulation velocity accelerates significantly from 4.33 m/s to 11.6 m/s. This flow acceleration is the result of a dual pumping mechanism within the closed-loop geometry. On one hand, the intensified centrifugal acceleration at higher speeds strongly propels the liquid condensate back from the condenser to the evaporator. On the other hand, this robust centrifugal return flow is coupled with the pressure-driven pumping action caused by continuous bubble generation and expansion in the evaporator, resulting in a significantly higher internal circulation velocity.

Consequently, one might expect that higher rotational speeds would continuously yield superior thermal performance due to the enhanced convective heat transfer and faster fluid circulation. However, the transient temperature response reveals a contradictory, non-monotonic behavior: the thermal performance improves up to an optimal speed (8500 rpm) but degrades at extreme speeds such as 10000 rpm.

This apparent paradox is resolved by examining the local thermodynamic state of the fluid, specifically the hydrostatic pressure distribution depicted in Fig. 14. This figure represents the hydrostatic pressure distribution resulting from centrifugal forces at various rotational speeds at 0.01 s. The selected time of 0.01 seconds was chosen to clearly display the developed hydrostatic pressure before significant thermal and mass transfer effects influence the pressure contours. In a high-speed rotating environment, the fluid at the outer radius (evaporator section) is subjected to an extreme hydrostatic pressure induced by the centrifugal force. Given the pressure-dependent nature of the saturation temperature, $T_{sat}(p)$, which was rigorously implemented in our numerical model, this surge in local pressure dramatically elevates the boiling point of liquid lithium at the evaporator walls.

At moderate rotational speeds (up to 8500 rpm), the benefit of enhanced centrifugal pumping outweighs the slight delay in boiling. The generated vapor bubbles are rapidly swept away, facilitating a vigorous two-phase flow and an efficient latent heat transport. Conversely, at ultra-high speeds (10000 rpm), the detrimental effect of the excessive hydrostatic pressure becomes the dominating physical mechanism initially. The elevated saturation temperature acts as a thermodynamic barrier, suppressing the nucleation of vapor bubbles and causing a temporal delay in the phase-change process. Although the fluid has a higher potential for rapid circulation (as evidenced by the 11.6 m/s velocity contour), the delay in vapor generation stalls the pulsatile action in the early stages.

As evident in the temperature-time plots, this thermodynamic barrier explains why the 10000-rpm case reaches the 2200 K threshold earlier than the optimal 8500 rpm case. However, a deeper analysis of the temperature trend (Fig. 11) reveals a crucial dynamic: although the 10000-rpm case initially lags behind all other configurations due to this delayed activation, it rapidly overtakes the lower speeds (2850 rpm and 3450 rpm) the moment boiling is finally initiated. It is predicted that if the exposure time were extended, the average focal track temperature at 10000 rpm would eventually drop below that of the 8500-rpm case, thereby extending the allowable operational time. This indicates that over longer durations, the long-term convective advantage of the maximized fluid circulation naturally overpowers the short-term penalty of the delayed nucleation induced by the hydrostatic pressure.

In conclusion, the thermal management efficacy of a lithium-based RPHP in rotating X-ray targets is governed by a delicate, time-dependent competition between mechanical pumping (centrifugal acceleration) and thermodynamic suppression (hydrostatic elevation of T_{sat}). The optimal rotational speed for a given pulse duration is defined by the sweet spot where fluid velocity is maximized without inducing a prohibitive delay in the boiling inception.

4.3. Internal Heat Spreading and Utilization of Thermal Capacitance

The ultimate objective of integrating an RPHP within the rotating X-ray target is to mitigate localized thermal stresses by efficiently dispersing the concentrated electron beam energy into the bulk material. Fig. 15 presents a direct comparison of the internal static temperature contours for the solid target (baseline) and the RPHP-integrated target at the optimal rotational speed of 8500 rpm, captured at the specific instant when each average temperature of focal track reaches a maximum temperature of 2200 K.

In the conventional solid target (Fig. 15 (a)), heat transfer is strictly governed by the thermal conductivity of the tungsten focal track and the underlying TZM molybdenum alloy (Fourier conduction). The thermal contour reveals a highly concentrated, shallow penetration zone beneath the focal track, resulting in a severe localized hot spot. The bulk of the TZM substrate remains thermally unengaged, effectively rendering its substantial sensible heat capacity underutilized during the short pulse duration.

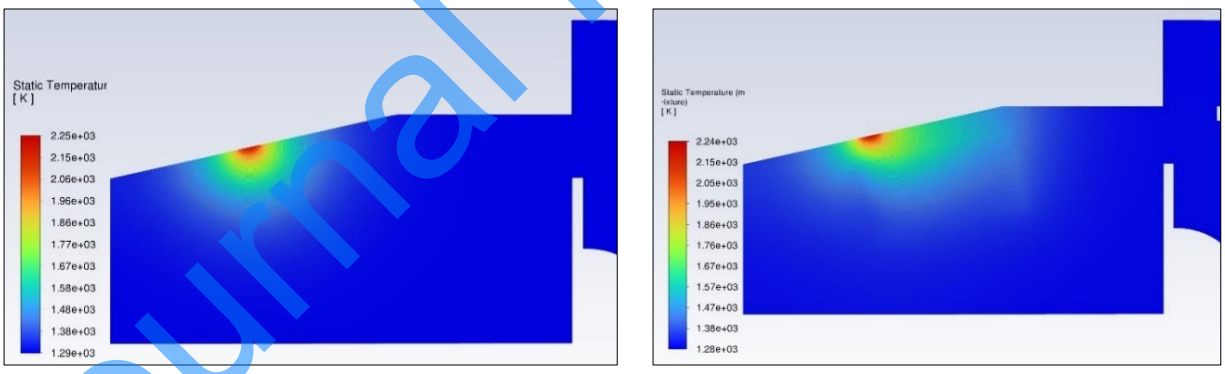

(a) **(b)**

Fig 15. Comparison of the anode temperature distribution at the end of the exposure time: (a) the baseline solid anode, and (b) the anode integrated with the lithium-based RPHP.

Conversely, the implementation of the lithium-based RPHP (Fig. 15 (b)) transforms the thermal landscape along its internal trajectory. The temperature contour clearly demonstrates a deep and rapid

penetration of thermal energy into the core of the TZM disk. Once the localized heat flux triggers the intense boiling of lithium in the evaporator section (as discussed in previous sections), the working fluid, driven by rapid phase change and vigorous flow circulation, transports the absorbed thermal energy (comprising both latent and sensible heat) towards the condenser section embedded deeper within the target.

This vigorous two-phase circulation bypasses the sluggish conductive thermal resistance of the solid metal. As a result, the RPHP acts as a high-efficiency internal heat spreader, actively drawing the intense heat away from the focal track and distributing it across a significantly larger volume of the TZM substrate. This internal heat spreading capability represents a paradigm shift in the thermal management of high-power rotating anodes, directly contributing to extended operational limits and prolonged tube lifespan.

5. Conclusion

This study numerically investigated the transient thermal behavior of a RAD-14 rotating anode X-ray tube equipped with an embedded lithium-filled Rotating Pulsating Heat Pipe (RPHP). A 3D VOF-based multiphase model with a pressure-dependent saturation temperature was developed to resolve rapid phase-change dynamics under extreme centrifugal loading. Applying a 20-kW heat pulse to the smallest focal spot (0.3 mm), the following key conclusions are drawn:

Extension of the Exposure Time: By enhancing latent and sensible heat transport into the deeper regions of the anode, the lithium RPHP successfully extended the allowable exposure time, defined by the 2200 K limit for the average focal track temperature, across all rotational speeds.

Time-Dependent Optimal Speed: The optimal rotational speed is governed by a dynamic competition between the time of bubble generation and fluid circulation velocity. Lower speeds (2850 and 3450 rpm) offer a brief initial advantage due to faster nucleation. However, 8500 rpm quickly becomes optimal for intermediate pulses, maximizing the pulse duration to 0.706 s (a 62%

enhancement over the solid baseline). For prolonged exposures 10000 rpm is predicted to outperform due to superior long-term fluid circulation, despite delayed initial boiling.

Conservative Predictions: The model's predictions are highly conservative. It assumes an initial temperature of 1300 K, whereas actual lithium oscillations begin at approximately 900 K. Additionally, the results were obtained using a conservative evaporation-condensation frequency of 1000 s^{-1}. Because theoretical phase change coefficients exceed this value, the real-world allowable exposure times will undoubtedly exceed these numerical estimates.

Risks Associated with Poor Phase-Change :As evidenced by the poor performance at low mass transfer frequencies, any disruption to the phase-change kinetics turns the RPHP into a thermal resistance rather than a cooling enhancer. To prevent this functional collapse, designers must strictly avoid non-capillary dimensions, extreme filling ratios, and high initial pressures caused by inadequate vacuuming or non-degassed inner surfaces. Furthermore, ultra-polished surfaces lacking nucleation cavities and surface impurities inducing hydrophobicity must be eliminated to ensure vigorous and continuous operation.

6. Future Work

In order to develop research and improve simulation, the following are suggested for future work:

The thermal resistance of the contact surface between the anode components should be considered in the simulation.

To increase accuracy, a periodic symmetric boundary condition should be used in the simulations.

Conflict of interest

The authors declare no conflicts of interest regarding this manuscript.

References

[1] Lee, S. M. (2015). Thermal characteristics of rotating anode X-ray tube with emissivity in aging process for digital radiography. *Applied Science and Convergence Technology*, 24(5), 125–131. https://doi.org/10.5757/ASCT.2015.24.5.125

[2] Bushong, S. C. (2013). *Radiologic Science for Technologists: Physics, Biology, and Protection*. (10th ed.). Mosby Elsevier.

[3] Lee, S. M. (2015). Compact anode design with the heat capacity performance in rotating anode x-ray tube for digital radiography. *Applied Science and Convergence Technology*, 24(5), 136-141.https://dx.doi.org/10.5757/ASCT.2015.24.5.136

[4] Li, X., Wang, X., Li, Y., & Liu, Y. (2020). Production and heat properties of an X-ray reflective anode based on a diamond heat buffer layer. *Materials*, 13(1), 241. https://doi.org/10.3390/ma13010241

[5] Taubin, M. L., Yaskolko, A. A., & Chesnokov, D. A. (2018). Thermal analysis of the focal spot of anodes of powerful X-ray tubes. *Biomedical Engineering*, 51, 328–331. https://doi.org/10.1007/s10527-018-9741-z

[6] Kumar, R., Ratnala, S. R., B, V. K. G., & Gouda, P. S. S. (2018). Thermal analysis on X-ray tube for exhaust process. *IOP Conference Series: Materials Science and Engineering*, 310, 012162. https://doi.org/10.1088/1757-899X/310/1/012162

[7] Pajovic, S., Roques-Carmes, C., Choi, S., Kooi, S. E., Gupta, R., Zalis, M. E., Čelanović, I., & Soljačić, M. (2025). Nanophotonic thermal management in X-ray tubes. *ACS Nano*, 19(95), 31363–31370. https://doi.org/10.1021/acsnano.5c08516

[8] Wang, Y., Jiang, S., Shi, S., & Yu, Y. (2025). Optimization design of heat dissipation structure for rotating anode CT tube based on simulation analysis. *Proceedings of the 2025 5th International Conference on Applied Mathematics, Modelling and Intelligent Computing (CAMMIC)*, 165–175. https://doi.org/10.1145/3754533.3754561

[9] Wang, Y., Jiang, S., & Shi, S. (2024). Thermal analysis on 3.5 MHU rotating anode X-ray. *2024 7th International Conference on Mechatronics, Computer Technology and Engineering (MCTE)*, 1334–1338. https://doi.org/10.1109/MCTE62870.2024.11778585

[10] Akachi, H., Structure of a Heat Pipe, US Patent No. 4921041 (issued 1990). Available at https://patents.google.com/patent/US4921041A/en (May 2026).

[11] Zhang, Y., & Faghri, A. (2002). Heat transfer in a pulsating heat pipe with open end. *International Journal of Heat and Mass Transfer*, 45(4), 755-764. https://doi.org/10.1016/S0017-9310(01)00203-4

[12] Khandekar, S., Dollinger, N., & Groll, M. (2003). Understanding operational regimes of closed loop pulsating heat pipes: an experimental study. *Applied Thermal Engineering*, 23(6), 707-719. https://doi.org/10.1016/S1359-4311(02)00237-5

[13] Khandekar, S., Charoensawan, P., Groll, M., & Terdtoon, P. (2003). Closed loop pulsating heat pipes part B: visualization and semi-empirical modeling. *Applied Thermal Engineering*, 23(16), 2021-2033. https://doi.org/10.1016/S1359-4311(03)00168-6

[14] Kwon, G. H., & Kim, S. J. (2014). Operational characteristics of pulsating heat pipes with a dual-diameter tube. *International Journal of Heat and Mass Transfer*, 75, 184-195. https://doi.org/10.1016/j.ijheatmasstransfer.2014.03.032

[15] Ebrahimi, M., Shafii, M. B., & Bijarchi, M. A. (2015). Experimental investigation on the thermal management of flat-plate closed-loop pulsating heat pipes with interconnecting channels. *Applied Thermal Engineering*, 90, 838-847. https://doi.org/10.1016/j.applthermaleng.2015.07.040

[16] Kwon, G. H., & Kim, S. J. (2015). Experimental investigation on the thermal performance of a micro pulsating heat pipe with a dual-diameter channel. *International Journal of Heat and Mass Transfer*, 89, 817-828. https://doi.org/10.1016/j.ijheatmasstransfer.2015.05.091

[17] Wang, J., Ma, H., Zhu, Q., Dong, Y., & Yue, K. (2016). Numerical and experimental investigation of pulsating heat pipes with corrugated configuration. *Applied Thermal Engineering*, 102, 158-166. https://doi.org/10.1016/j.applthermaleng.2016.03.163

[18] Frey, Y., Dörr, A., & Lorenz, M. (2023). Experimental investigation of pulsating heat pipes with different evaporator roughness values. *Applied Thermal Engineering*, 233, 120999. https://doi.org/10.1016/j.applthermaleng.2023.120999

[19] Yu, R. Li., Wang, X. Y., Jiao, D. S., Qi, R. D., Wang, Z. H., Li, Z. L., Zhu Q. R., & Xia, L. Z. (2025). Effect of improving the performance of pulsating heat pipes on heat transfer in an extruder. *Experimental and Computational Multiphase Flow*, 7, 537–550. https://doi.org/10.1007/s42757-024-0211-4

[20] Hong, Y., Kang, Z., & Fan, J. (2025). Heat transfer enhancement of pulsating heat pipes with novel structures. *Applied Thermal Engineering*, 268, 125720. https://doi.org/10.1016/j.applthermaleng.2025.125720

[21] Moayad, N. A., & Sarsam, W. S. (2026). Thermal performance of a pulsating heat pipe heat exchanger for energy recovery in air conditioning systems in a high ambient temperature country. *Journal of Engineering and Applied Science*, 73, 47. https://doi.org/10.1186/s44147-026-00897-9

[22] Aboutalebi, M., Moghaddam, A. M. N., Mohammadi, N., & Shafii, M. B. (2013). Experimental investigation on performance of a rotating closed loop pulsating heat pipe. *International Communications in Heat and Mass Transfer*, 45, 137–145. https://doi.org/10.1016/j.icheatmasstransfer.2013.04.008

[23] Kammuang-lue, N., Phommavongsa, D., On-ai, K., Sakulchangsatjatai, P., & Terdtoon, P. (2016). Thermal resistance of a rotating closed-loop pulsating heat pipe: Effect of centrifugal accelerations. *Applied Mechanics and Materials*, 851, 292-298. https://doi.org/10.4028/www.scientific.net/AMM.851.292

[24] Qian, N., Fu, Y., Zhang, Y., Chen, J., & Xu, J. (2019). Experimental investigation of thermal performance of the oscillating heat pipe for the grinding wheel. *International Journal of Heat and Mass Transfer*, 136, 904-915. https://doi.org/10.1016/j.ijheatmasstransfer.2019.03.065

[25] Ebrahimi Dehshali, M., Nazari, M. A., & Shafii, M. B. (2018). Thermal performance of rotating closed-loop pulsating heat pipes: Experimental investigation and semi-empirical correlation. *International Journal of Thermal Sciences*, 123, 14-26. https://doi.org/10.1016/j.ijthermalsci.2017.09.009

[26] Gao, Y., Xu, Z., Zhai, E., Liang, K., Zhao, R., Li, H., Wang, L., Liu, S., & Li, X. (2023). Cooling pitch cabinets in wind turbines using a pulsating heat pipe: A case study. *Case Studies in Thermal Engineering*, 50, 103461. https://doi.org/10.1016/j.csite.2023.103461

[27] Behling, R., Hulme, C., Tolias, P., & Danielsson, M. (2025). The impact of tube voltage on the erosion of rotating x-ray anodes. *Medical Physics*, 52(2), 814–825. https://doi.org/10.1002/mp.17528

[28] Siller, M., Gamerdinger, M., Evers, T., Schatte, J., Gerzoskovitz, S., Olschok, S., Reisgen, U., & Mark, M. (2026). Focal track wear of rotating anodes: Revealing the interaction of the microstructure, surface degradation, and resulting changes in X-ray emission. *International Journal of Refractory Metals and Hard Materials*, 139, 107854.

[29] Suresh, J. V., & Bhramara, P. (2018). CFD analysis of copper closed loop pulsating heat pipe. *Materials Today: Proceedings*, 5(2), 5487–5495. https://doi.org/10.1016/j.matpr.2017.12.138

[30] Wang, S. F., Lin, Z. R., Lee, Z. Y., & Zhang, L. W. (2012). Numerical simulation on flow and heat transfer in oscillating heat pipes. *Frontiers in Heat Pipes*, 3(1), 013002. https://doi.org/10.5098/fhp.v3.1.3002

[31] Wang, J., Wang, Z., & Li, M. (2014). Thermal performance of pulsating heat pipes with different heating patterns. *Applied Thermal Engineering*, 64(1-2), 209-212. https://doi.org/10.1016/j.applthermaleng.2013.12.004

[32] Suresh, J. V., & Bhramara, P. (2017). CFD analysis of multi turn pulsating heat pipe. *Materials Today: Proceedings*, 4(2), 2701-2710. https://doi.org/10.1016/j.matpr.2017.02.146

[33] Pouryoussefi, S. M., & Zhang, Y. (2017). Analysis of chaotic flow in a 2D multi-turn closed-loop pulsating heat pipe. *Applied Thermal Engineering*, 126, 1069–1076. https://doi.org/10.1016/j.applthermaleng.2017.01.097

[34] Lin, Y. H., Kang, S. W., & Wu, T. Y. (2009). Fabrication of polydimethylsiloxane (PDMS) pulsating heat pipe. *Applied Thermal Engineering*, 29(2-3), 573-580. https://doi.org/10.1016/j.applthermaleng.2008.03.028

[35] Varian Medical Systems. *RAD-14 X-Ray Tube* (Rev. M). https://www.yumpu.com/fr/document/read/4465693/rad-14-rev-m-varian (Access June 2024)

[36] ANSYS Inc. (2024). *ANSYS Fluent Theory Guide* (Release 2024 R2). ANSYS Inc. http://ansyshelp.ansys.com/public/account/secured? (Access May 2026)

[37] Lee, W. H. (1979). *A Pressure Iteration Scheme for Two-Phase Modeling* (Technical Report LA-UR-79-975). Los Alamos Scientific Laboratory. https://codethatflows.wordpress.com/wp-content/uploads/2021/08/406441216-lee-model-pdf-1.pdf (Access May 2026)

[38] Brackbill, J. U., Kothe, D. B., & Zemach, C. (1992). A continuum method for modeling surface tension. *Journal of Computational Physics*, 100(2), 335-354. https://doi.org/10.1016/0021-9991(92)90240-Y

[39] Chen, G., Nie, T., & Yan, X. (2020). An explicit expression of the empirical factor in a widely used phase change model. *International Journal of Heat and Mass Transfer*, 150, 119279. https://doi.org/10.1016/j.ijheatmasstransfer.2019.119279

[40] Mo, Z. Y., & Xie, G. (2020). An assessment and analysis of phase change models for the simulation of vapor bubble condensation. *International Journal of Heat and Mass Transfer*, 157, 119924. https://doi.org/10.1016/j.ijheatmasstransfer.2020.119924

[41] Ma, H. (2015). *Oscillating Heat Pipes* (first ed.) Springer New York, NY. https://doi.org/10.1007/978-1-4939-2504-9

[42] Incropera, F. P., DeWitt, D. P., Bergman, T. L., & Lavine, A. S. (2006). *Fundamentals of Heat and Mass Transfer* (6th ed.). John Wiley & Sons.

[43] Wieland Duro. *TZM Technical Data Sheet*. https://www.wieland.com/fr/content/download/12678/file/TZM_EX_EN.pdf (Acesss May 2026).

[44] Park, Y. H., Tanshen, M. R., Nine, M. J., Chung, H. S., & Jeong, H. M. (2012). Characterizing pressure fluctuation into single-loop oscillating heat pipe. *Journal of Central South University*, 19, 2578–2583. https://doi.org/10.1007/s11771-012-1313-x